JOM, Vol. 74, No. 5, 2022
https://doi.org/10.1007/s11837-022-05254-8

Oscillating Currents Stabilize Aluminum Cells for Efficient, Low Carbon Production

IBRAHIM MOHAMMAD [1], MARC DUPUIS,[2] PAUL D. FUNKENBUSCH [1], and DOUGLAS H. KELLEY [1,3]

1.—Department of Mechanical Engineering, University of Rochester, Rochester, NY 14627, USA. 2.—GeniSim Inc., Jonquière, QC G7S 2M9, Canada. 3.—e-mail: d.h.kelley@rochester.edu

The electrolytic current in an aluminum smelter can amplify resonant motions on the Al–electrolyte interface, producing a circulating wave that can grow out of control. Thick electrolyte layers prevent this magnetohydrodynamic metal pad instability (MPI) but sacrifice efficiency because the electrolyte is a poor conductor. In high-fidelity simulations of a TRIMET 180 kA smelter, we found that adding an oscillating component to the current prevented the MPI and replaced it with stable standing waves. We also found that initiating an oscillating current component can halt the MPI in progress. In our simulations, stable operation with steady current required a 4.3-cm anode–cathode distance (ACD), but stable operation with oscillations was achieved at 3.8 cm ACD, with heat power reduced by 12% and overall power by 4%. Different frequencies or amplitudes might allow further ACD reduction. Our method could allow Al production at lower cost, with less energy, and a smaller carbon footprint.

INTRODUCTION

Aluminum is produced using Hall–Héroult electrolysis cells that contain two broad ($\sim 8 \times 3.6$ m, or larger) and shallow fluid layers ($\sim 5-20$ cm): molten Al beneath a floating layer of molten cryolite electrolyte, in which raw aluminum oxide is dissolved. A large, steady current ($\sim 10^5$ A) is driven downward from a carbon anode at the electrolyte surface to a cathode beneath the aluminum (Fig. 1a), reducing the aluminum oxide to Al and producing carbon dioxide (CO_2), an important greenhouse gas, at the anode. Substantially more CO_2 is emitted when generating the necessary electricity, most of which comes from fossil fuels.[1] Of the 51 Gton/year of CO_2-equivalent (CO2e) emissions produced by humankind,[2] 1% comes from Al production,[3] and 62% of that from the electricity.[1] To meet growing global demand while decreasing the CO_2 emissions that exacerbate climate change, it is critical to increase the energy efficiency of Al production.

About 40% of a cell's electrical energy reduces no Al,[4] instead being transformed into heat by resistance in the electrolyte, which is four orders of magnitude less conductive than Al. Being approximately proportional to the electrolyte layer thickness, quantified by the anode–cathode distance (ACD), this loss can be decreased by squeezing the ACD. However, when the ACD is decreased below a certain critical threshold, the cell becomes unstable.[5–11] In a process known as metal pad instability (MPI),[12] electromagnetic forces amplify small perturbations on the Al–electrolyte interface, causing a circulating traveling wave that can grow exponentially until the cell sloshes out of control or the Al shorts to the anode. To predict the threshold, multiple theories have been proposed,[5,6,8,13,14] depending in part on the uniformity of the ambient vertical magnetic field (Fig. 1b). In all the theories, magnetohydrodynamic instability imposes a minimum ACD. Many methods for MPI suppression have been attempted in the past, including inserting baffles in the Al layer[4,15] or tilting the anode in synchrony with the interface motion,[4] but with

This work was supported by the National Science Foundation (CBET-1552182) and by a University of Rochester, URVentures TAG award.

(Received September 20, 2021; accepted March 2, 2022; published online April 1, 2022)

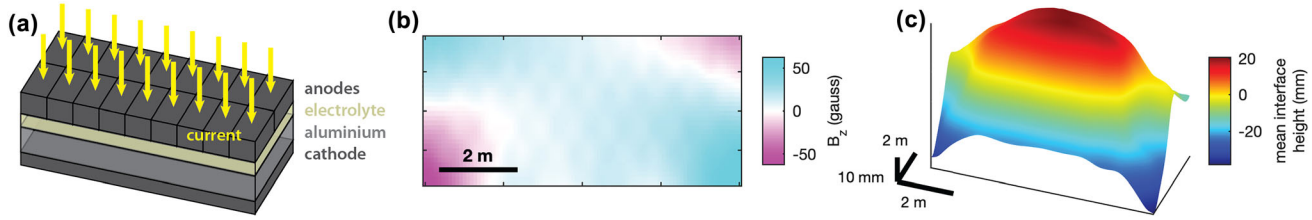

Fig. 1. Characteristics of Al electrolysis cells: (a) electrical current flows downward from anodes to cathode, through the electrolyte and Al layers; (b) the vertical component of the ambient magnetic field, at the Al–electrolyte interface, from our simulations, seen from above; the field varies spatially and is caused primarily by currents in the cell and nearby busbars; (c) the Al–electrolyte interface bulges because of electromagnetic forces due to the magnetic field and the current

limited success. In practice, the MPI is mitigated by keeping the ACD thick and building cells with greater length L_x than width L_y. Certain aspect ratios L_x/L_y, especially those near 2.1, hinder the MPI[14] because it is a parametric instability that depends on a coupled resonance between the interface wave modes.[16] The height of the Al–electrolyte interface varies spatially, and can be written in terms of the wave modes as:

$$\sum_{m,n} \alpha_{m,n} G_{(m,n)} = \sum_{m,n} \alpha_{m,n} \cos\left(\frac{m\pi}{L_x}\left(x+\frac{L_x}{2}\right)\right) \cos\left(\frac{n\pi}{L_y}\left(y+\frac{L_y}{2}\right)\right) \tag{1}$$

where $G_{(m,n)}$ is an interface mode, $\alpha_{m,n}$ is its amplitude, (m, n) are non-negative integers, x increases along the long axis of the rectangular cell, y increases along its short axis, and $(x,y)=(0,0)$ at the center of the cell. Each $G_{(m,n)}$ has the form of a standing wave whose temporal frequency nearly matches the corresponding hydrodynamic gravity wave mode, whose frequency $f_{m,n}$[17] is independent of current and (at the limit of shallow cells) is given by:

$$f_{m,n}^2 = \frac{(\rho_{Al}-\rho_c)g}{2\pi\left(\frac{\rho_{Al}}{h_{Al}}+\frac{\rho_e}{h_e}\right)}\left[\left(\frac{m\pi}{L_x}\right)^2+\left(\frac{n\pi}{L_y}\right)^2\right] \tag{2}$$

where $\rho_{Al}, \rho_e, h_{Al}$, and h_e are the densities and thicknesses of the Al and electrolyte, respectively. When two modes have nearly identical frequencies and cause surface motion at right angles (e.g., one with $m = 0$, another with $n = 0$), their resonant coupling can give rise to the MPI.[11] As Eq. (2) shows, if $L_x/L_y = 1$, frequencies of $m = 0$ and $n = 0$ modes match exactly; accordingly, the MPI is predicted to occur even with arbitrarily thick electrolyte layers in square or circular cells. If $L_x/L_y \approx 2.1$, as in many commercial Al reduction cells, $n = 0$ modes have lower frequencies than $m = 0$ modes, and the MPI can be avoided if the ACD is kept thick, at the expense of reduced energy efficiency and increased carbon emissions.

In this work, we propose a novel method for preventing the MPI in Al reduction cells: adding an oscillating current component to the reduction current. We present a suite of numerical results from simulating a Trimet 180 kA Al cell in MHD-Valdis software. We first show that the MPI is present at 4-cm ACD, where the interface displacement is a circulating wave growing exponentially in time. Looking at the power spectrum of the displacement of a point on the interface, we find a spectral peak at the MPI frequency. By projecting the interface displacement onto the set of modes $G_{(m,n)}$, we find which modes are strongest and explain the different mode couplings through the horizontal electromagnetic forces that result in the MPI. Then, we show that adding an oscillating current component, with a particular amplitude and frequency, to the 4-cm ACD cell makes it stable where the interface displacement is a standing wave. Analyzing the interface displacement shows an additional spectral peak at the oscillating current's frequency and that the strongest modes correspond to ones whose frequency also nearly matches the current's frequency. We believe that the oscillating current is driving the standing waves and give a simple mechanism of how the standing waves suppress the MPI.

MPI AND INTERFACE MODE COUPLINGS

We simulated the MPI in a TRIMET 180 kA Al reduction cell[18] using the MHD-Valdis software[18–20] (see Methods, Supplementary Table S-1). The Al–electrolyte interface developed a central bulge (Fig. 1c) as expected. The cell was stable with a steady, 180-kA current when the ACD was 4.3 cm (Supplementary Fig. S-1, refer to online supplementary material). With ACD = 4.0 cm, however, the MPI rose (Supplementary Video S-1). We quantified MPI magnitude using the root-mean-square (RMS) vertical displacement of the surface from its average shape (see Methods), which has low-frequency dynamics consistent with exponential growth (Fig. 2a). Oscillation was also evident, so we calculated the power spectrum of the displacement at a point, finding its power to be highly

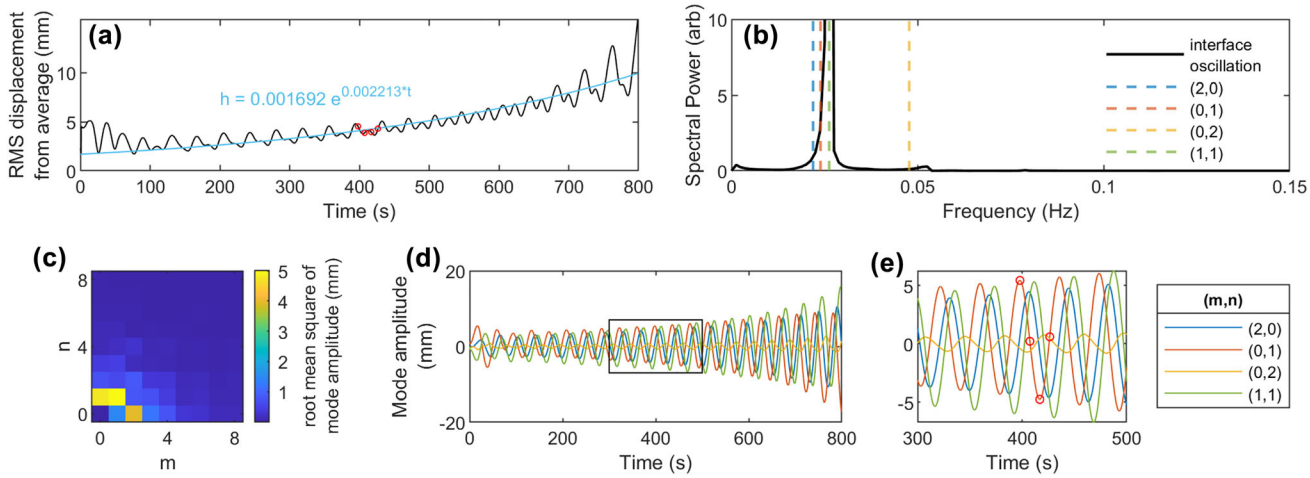

Fig. 2. The metal pad instability (MPI) in a simulated Al electrolysis cell: (a) displacement of the Al–electrolyte interface grows exponentially, as shown by the fitted curve; (b) the spectral power of the displacement of one point on the interface is dominated by a narrow frequency band, close to the gravitational wave modes $G_{(2,0)}$, $G_{(0,1)}$, and $G_{(1,1)}$, expected in the MPI; (c) $G_{(2,0)}$, $G_{(0,1)}$, and $G_{(1,1)}$ have greater RMS amplitude than any other modes; (d) $G_{(2,0)}$, $G_{(0,1)}$, $G_{(1,1)}$, and $G_{(0,2)}$ oscillate with a common frequency and grow over time; and (e) $G_{(2,0)}$ and $G_{(0,1)}$ are separated in phase by $\sim 90^\circ$, characteristic of a traveling wave as in the MPI

concentrated near 0.0263 Hz (Fig. 2b), close to $f_{2,0}$, $f_{0,1}$, and $f_{1,1}$, the frequencies of the modes whose coupling is expected to produce the MPI.[11] To verify the role of those three modes, we performed a least-squares projection of the simulated interface shape onto a basis set of gravity modes $G_{(m,n)}$, then calculated the RMS amplitude $\langle \alpha_{m,n} \rangle^{\frac{1}{2}}$ of each mode, through the duration of the simulation (Fig. 2c; see Methods). As expected, $G_{(2,0)}$, $G_{(0,1)}$, and $G_{(1,1)}$ are far stronger than all other modes. Their amplitudes $\alpha_{m,n}$ grow exponentially over time and oscillate with frequencies near 0.0263 Hz (Fig. 2d, e).

To explain the different mode couplings, we express the vertical magnetic field B_z (Fig. 1b) as a Taylor series:

$$B_z = B_{0z} + B_{xz}x + B_{yz}y, \tag{3}$$

where B_{0z} is the uniform component, B_{xz} quantifies linear variation in the x direction, B_{yz} quantifies linear variation in the y direction, and higher-order terms have been neglected. In commercial potlines B_{0z} is generated primarily by the current in the adjacent line, B_{xz} is generated primarily by the current in the side risers and busbar under the cell, and B_{xy} is generated primarily by current in the anode risers or cathode busbar.[11] When a wave is present on the Al–electrolyte interface, current flows preferentially where the electrolyte is thinner (at interface crests), then spreads horizontally after entering the Al layer. That spreading creates a horizontal compensation current density, j, in the Al pointing from a crest to a trough, which interacts with the different components of B_z to create horizontal electromagnetic forces, f, that couple different modes.[6,8,11] For example, the $G_{(0,1)}$ mode causes a horizontal current density, j, that interacts with B_{xz} to produce a force, f, that excites the $G_{(2,0)}$ mode (Fig. 3a). It, in turn, excites the $G_{(0,1)}$ mode, resulting in a feedback loop (Fig. 3b–d). Similarly, B_{0z} couples the $G_{(2,0)}$ and $G_{(1,1)}$ modes (Fig. 3e, h), and B_{yz} couples the $G_{(0,1)}$ and $G_{(1,1)}$ modes (Fig. 3I, l).

Visualizing the interface displacement shape at four times spaced evenly through a 0.0263-Hz oscillation cycle reveals canonical MPI dynamics: a traveling wave that circulates counter-clockwise when viewed from above (Fig. 4a–d), consistent with the fact that $G_{(2,0)}$ and $G_{(0,1)}$ vary with $\sim 90^\circ$ phase difference. To understand the underlying MPI mechanism, a simplified representation is helpful, so we first found which modes are present each instant (Fig. 4e–h) by calculating the mode's amplitude as a percentage of the total energy of all modes. Here, we quantified the total energy of all modes by the sum of all the modes' amplitudes in absolute values. The sign of the mode amplitude was preserved to indicate the mode orientation. Then, we reconstructed the interface shape after eliminating all but the two strongest modes at each instant (Fig. 4I–l). With the aid of the coupling mechanisms presented in Fig. 3, we can see the interplay between $G_{(0,1)}$, $G_{(2,0)}$, and $G_{(1,1)}$; the most dominant modes present (Fig. 2b, c). At $t = 398s$, $G_{(0,1)}$ and $-G_{(1,1)}$ are present and excite $G_{(2,0)}$ and $G_{(1,1)}$, which have appeared by $t = 407.5s$. Those modes, in turn, excite $-G_{(0,1)}$ and $G_{(1,1)}$, which have appeared by $t = 417s$. Those modes, in turn, excite $-G_{(2,0)}$ and $-G_{(1,1)}$, which have appeared by $t = 426.5s$. Finally, they excite the original modes, $G_{(0,1)}$ and $-G_{(1,1)}$. The coupling and timing of the three modes are right for forming a closed cycle that amplifies the circulating wave.

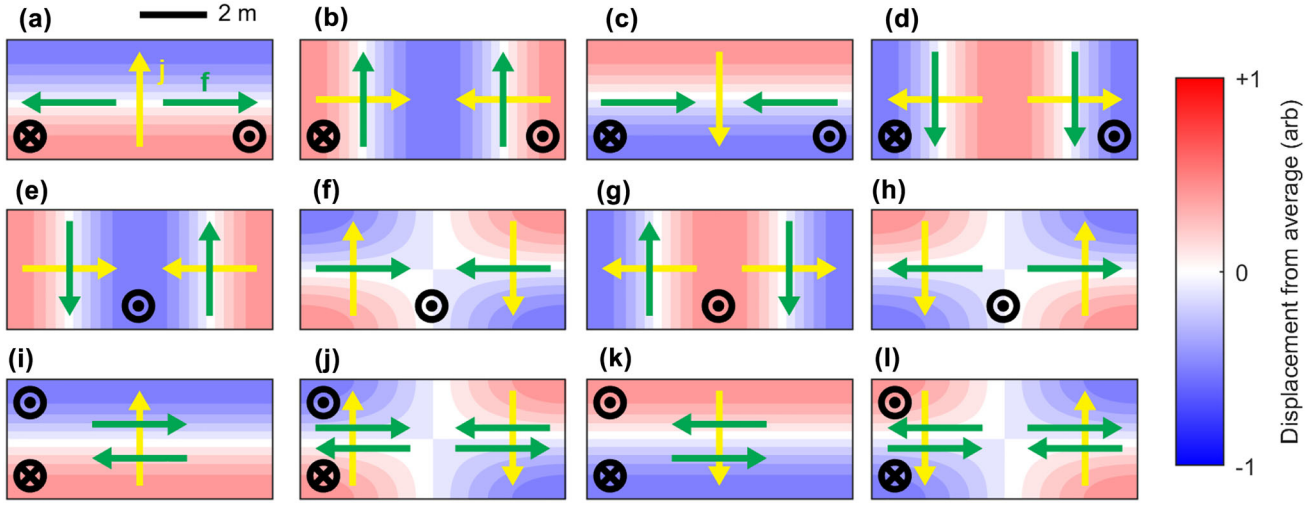

Fig. 3. Coupling of different mode pairs through the magnetic field components: (a–d) coupling between $G_{(0,1)}$ and $G_{(2,0)}$ interface modes through the x-gradient component B_{xz} of the vertical magnetic field B_z; the modes are viewed from above, with the horizontal displacement current density, j, and resulting electromagnetic forces, f, sketched; (e–h) coupling between $G_{(2,0)}$ and $G_{(1,1)}$ interface modes through the constant component B_{0z} of B_z; (i–l) coupling between $G_{(0,1)}$ and $G_{(1,1)}$ interface modes through the y-gradient component B_{zy} of B_z

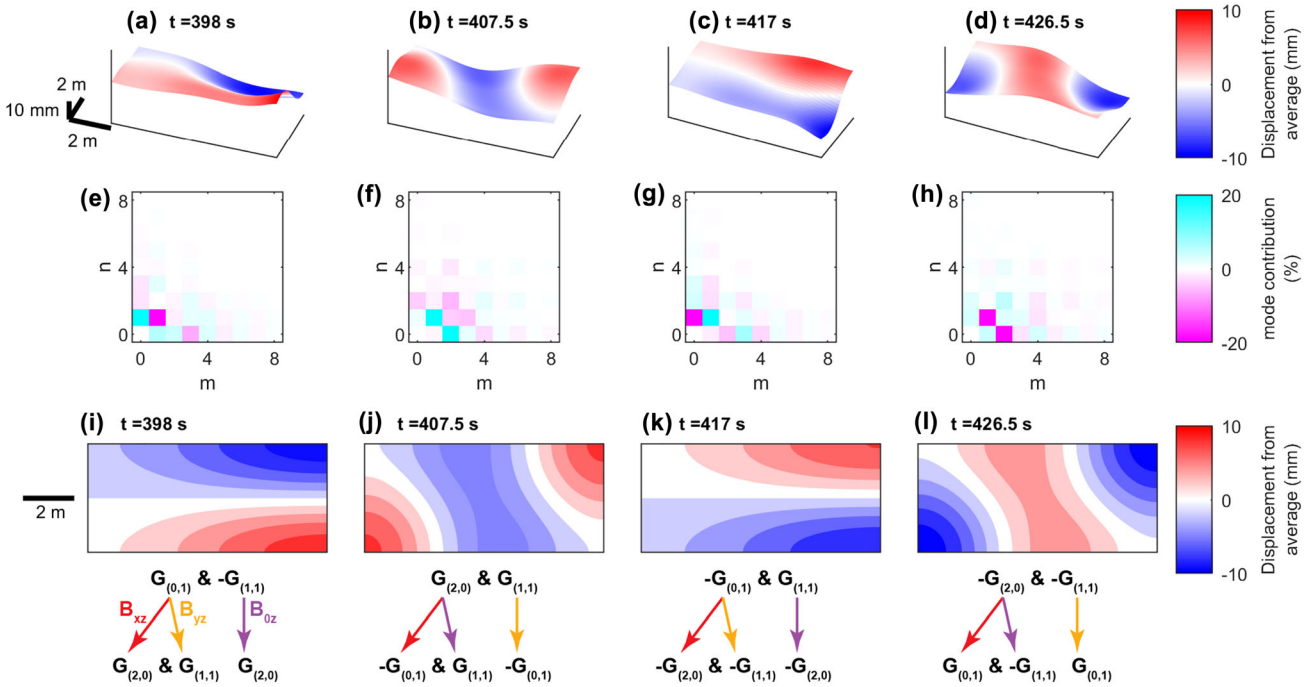

Fig. 4. Mode coupling creating the MPI; (a–d) interface displacements at four times spanning one MPI cycle (red dots in Fig. 2(e)) show a circulating traveling wave; (e–h) modal decomposition of the interface displacements at the same times as in (a–d); two dominant modes are present at each time, and an interplay between $G_{(2,0)}$, $G_{(0,1)}$, and $G_{(1,1)}$ is evident in creating the MPI; (i–l) reconstruction of the interface displacements at the same times as in (a–d) using only the two most dominant modes present in each of (e–h), viewed from above; $G_{(0,1)}$ and $-G_{(1,1)}$ are present in (l) and excite $G_{(2,0)}$ and $G_{(1,1)}$ through the different components of B_z based on Fig. 3; $G_{(2,0)}$ and $G_{(1,1)}$ consequently excite $-G_{(0,1)}$ and $G_{(1,1)}$ and so on (Color figure online)

STABILIZATION USING AN OSCILLATING CURRENT

Parametric instabilities can often be decoupled by introducing a new frequency that frustrates the resonance, so we hypothesized that adding an oscillation to the current would prevent the MPI. To test this, we ran a new simulation, identical to the one that produced the MPI, except that the steady 180-kA current was supplemented with an oscillating component of half-amplitude 19.8 kA and frequency 0.045 Hz. Although the RMS interface displacement oscillated, it did not grow exponentially; the MPI was absent (Fig. 5a, Supplementary Video S-2). The spectral power of the displacement

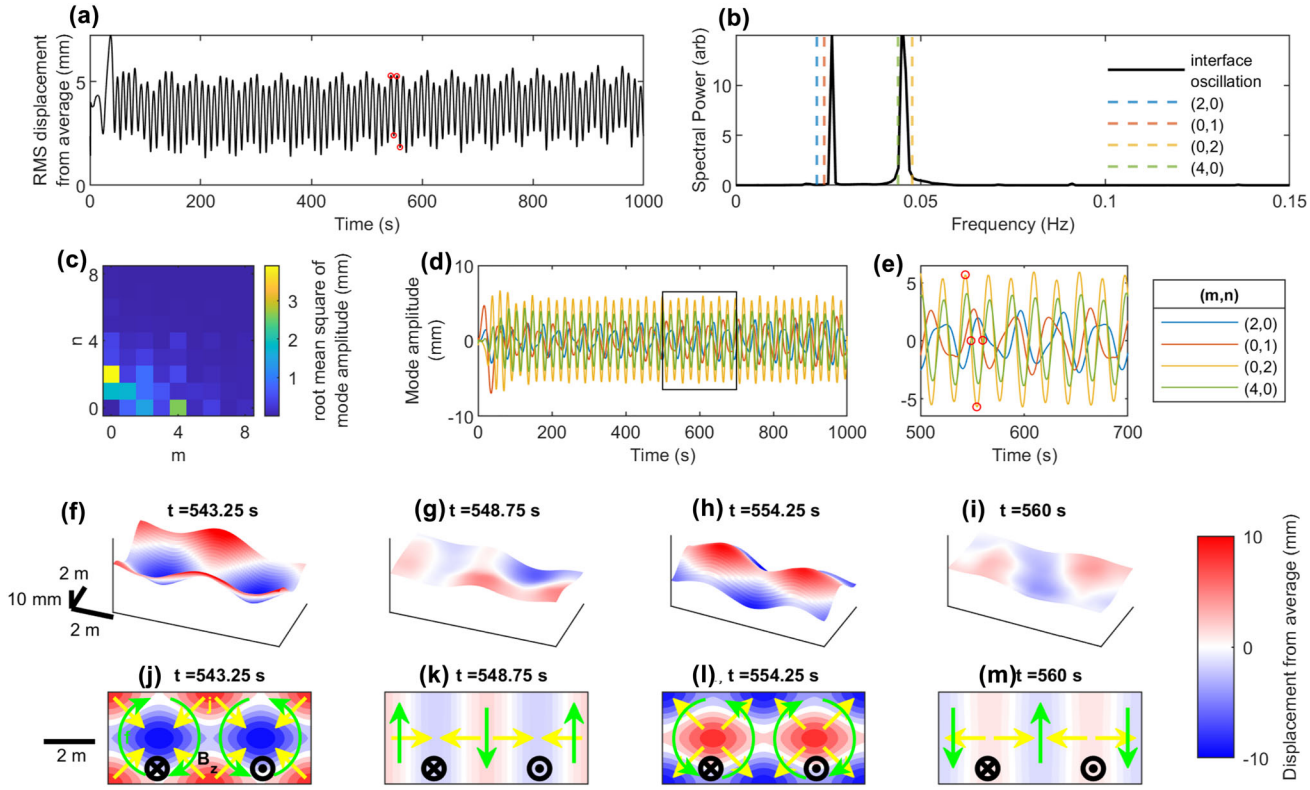

Fig. 5. An oscillating current component prevents the MPI: (a) the Al–electrolyte interface oscillates stably; (b) the spectral power of the displacement of one point on the interface is dominated by one frequency band close to the expected in the MPI frequency, and another close to the drive frequency; (c) $G_{(2,0)}$, $G_{(1,0)}$, $G_{(0,2)}$, and $G_{(4,0)}$ have greater RMS amplitude than any other modes; (d, e) their amplitudes $\alpha_{m,n}$ oscillate, and $G_{(0,2)}$ and $G_{(4,0)}$ are almost aligned in phase, characteristic of a standing wave; (f–i) interface displacements at four times spanning one drive cycle (red dots in (e)) show a standing wave; (j–m) interface displacements at the same times as in (f–i), estimated using only $G_{(0,2)}$ and $G_{(4,0)}$ and viewed from above; the resulting electromagnetic forces, f (sketched), often favor clockwise circulation, opposing and frustrating the MPI (Color figure online)

at a point showed strong peaks at two frequencies, one near $f_{2,0}$, $f_{0,1}$, and $f_{1,1}$, as seen in the presence of the MPI, and another near the 0.045-Hz drive frequency (Fig. 5b). Decomposing the interface shape into wave modes, we found that, in addition to $G_{(2,0)}$, $G_{(0,1)}$, and $G_{(1,1)}$, $G_{(0,2)}$ and $G_{(4,0)}$ were also strong (Fig. 5c). Their frequencies $f_{0,2}$ and $f_{4,0}$ nearly match the drive frequency (Fig. 5b), and the temporal variations of their amplitudes $\alpha_{m,n}$ are nearly sinusoidal (Fig. 5d, e), unlike those of $G_{(2,0)}$ and $G_{(0,1)}$, which are more complicated. Visualizing the interface shape at four times spaced evenly through a 0.045-Hz oscillation cycle reveals not a traveling wave, as would occur with the MPI, but a standing wave (Fig. 5f–I), consistent with the fact that $G_{(0,2)}$ and $G_{(4,0)}$ vary synchronously and with almost no phase difference (Fig. 5e). Taken together, these facts suggest that a standing gravity wave, driven by the current oscillation, frustrates the circulating wave that comprises the MPI.

For a simplified explanation of the mechanism, we reconstructed the interface shape after eliminating all modes except $G_{(0,2)}$ and $G_{(4,0)}$, which account for most of the power and can approximate the actual shape well (Fig. 5j–m). Remembering that current in the Al spreads horizontally from interface crests, we see that the resulting electromagnetic forces tend to drive two vortex-like circulations, one in each half of the cell, whose vorticities alternate over time but are always opposed: one clockwise and one counter-clockwise. Although counter-clockwise flow might tend to facilitate the counter-clockwise MPI circulation (even if not near the cell center), clockwise flow strongly opposes the MPI and is apparently sufficient, in this case, to prevent it altogether.

These observations suggest a novel strategy for stabilizing Al cells[21]: oscillate the current at a frequency chosen to excite standing wave modes, which frustrate the MPI traveling wave. In addition to the standing wave composed of the $G_{(0,2)}$ and $G_{(4,0)}$ modes, we reasoned that other standing wave modes, composed of other $G_{(m,n)}$ pairs with approximately matched $f_{m,n}$, should also work. In another simulation, we prevented the MPI using a current oscillation of 19.8 kA at 0.069 Hz, exciting $G_{(0,2)}$ and $G_{(6,0)}$ (Supplementary Figure S-2; Supplementary Video S-3). In another, again using 19.8 kA and 0.045 Hz, we prevented the MPI even with 3.8-cm ACD, demonstrating at least a 12% reduction from

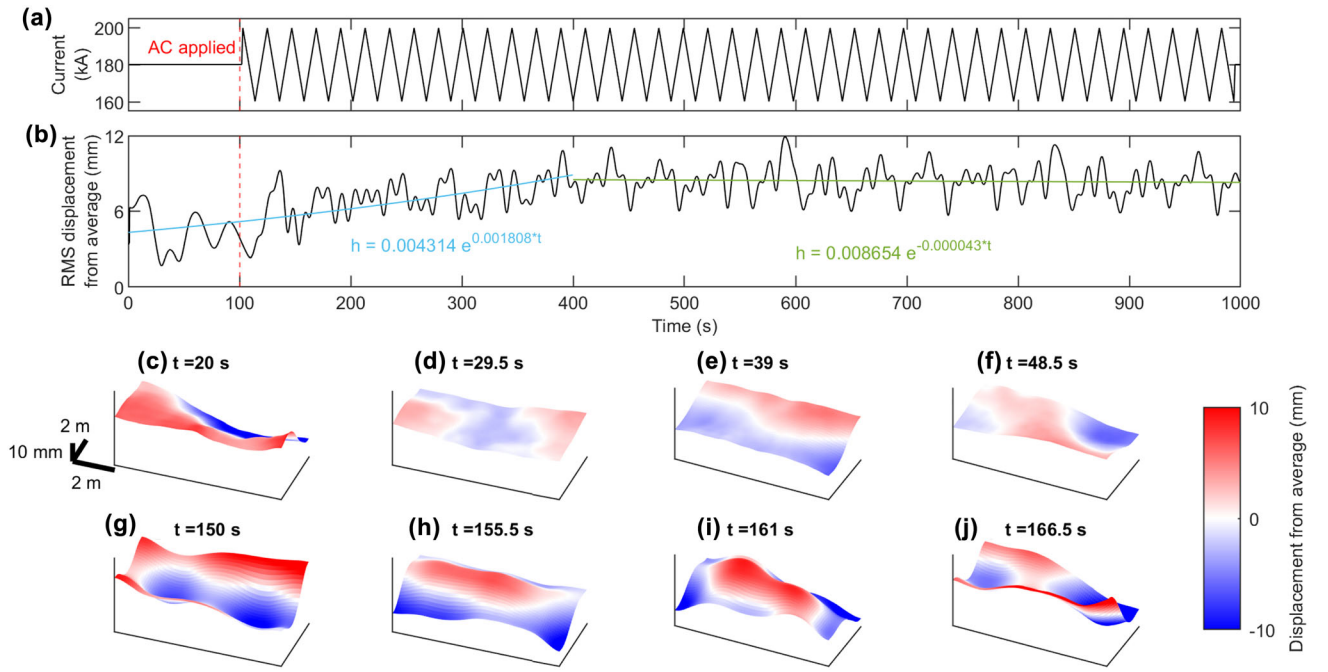

Fig. 6. An oscillating current component halts the MPI in progress: (a) the applied current was steady for the first 100 s, before an oscillatory current of 19.8 kA at 0.045 Hz was added; (b) interface displacement grew when the current was steady but stopped growing soon after we added current oscillation, indicating stability; (c–f) interface displacements at four times spanning one MPI cycle, when current was steady, show a circulating traveling wave; (g–j) interface displacements at four spanning one drive cycle, after we added oscillation, show a standing wave

the thickness required for stability without oscillation is possible. (Supplementary Figure S-3; Supplementary Video S-4). As expected, the average ohmic losses varied approximately linearly with ACD and were reduced 12%. Total average power, which also includes the power unavoidably necessary for electrolysis, was reduced 4% (Supplementary Figure S-4), compared to the case that was stable without current oscillation.

Having prevented the MPI, we wondered if we could also halt it in progress. To find out, we simulated with 4.0-cm ACD, holding the current steady at 180 kA for 100 s before adding a 19.8-kA oscillation at 0.045 Hz (Fig. 6a). As expected, the RMS displacement grew when the current was steady but stopped growing soon after we applied the current oscillation (Fig. 6b; Supplementary Video S-5). The interface moved with the characteristics of the MPI when the current was steady, but with the characteristics of standing waves after we applied the current oscillation (Fig. 6c–g, j). The MPI was apparently halted.

CONCLUSION

By applying oscillating currents to excite standing waves, we have both prevented and halted the MPI in simulations of TRIMET 180 kA Al reduction cells. Currently in commercial use by TRIMET Aluminum in Germany, these cells normally operate at 4.5-cm ACD and have been simulated in previous studies that validated the model with real-world measurements.[18–20] Other cell designs differ in, e.g., busbar configuration (affecting B_z),[22–24] size (affecting $f_{m,n}$), and aspect ratio (affecting which modes couple, in the MPI and in standing waves). Still, standing waves composed of low-order modes can be excited in any design by oscillating the current at a frequency determined using Eq. (2), and those standing waves will impose clockwise forces that oppose the MPI much of the time; our novel stabilization strategy is broadly applicable. For a given design, many standing wave modes are possible, but we speculate that the lowest-frequency mode will be strongest for a given oscillation amplitude, because viscous damping is weaker for low-frequency modes. Thus, we hypothesize that low-frequency modes frustrate the MPI with minimal oscillation amplitude; we hope to test that hypothesis in future work. With additional simulations, we found that, although the MPI can be prevented with 19.8-kA oscillation, it cannot be prevented with 3.6-kA oscillation. In future work, we hope to prevent the MPI with smaller oscillations. Other designs have been more carefully optimized, allowing stable operation with steady currents and ACD < 3 cm.[25] Still, decreasing the ACD in any design could enable producing aluminum with less energy, lower cost, and lower emissions. We hope to test our strategy in an industrial-scale Al cell soon.

Producing the large oscillating currents that we have simulated will require power electronics of substantial cost, but we expect that, in nearly all

cases, achieving the same efficiency increase by busbar reconfiguration or pot redesign would cost far more. Decreasing ACD by 12% and total power by 4% in all Al reduction cells could reduce the energy intensity of production by 2.1 MJ/kg Al, bringing annual savings of 34 TWh of electricity, perhaps US$1B in energy costs and 13 Mt of CO2e emissions. Future work may yield bigger decreases. Given that the MPI is likely to occur in liquid metal batteries (a grid-scale energy storage technology)[26–28] and molten oxide electrolysis cells (for electrochemical manufacture of iron and other metals),[29,30] it may be useful to also apply oscillating currents in those systems.

METHODS

Simulation Software

To study the stability of a typical aluminum reduction cell under the influence of an oscillating current, we used the simulation package MHD-Valdis, a tool widely used in the industry to design stable aluminum reduction cells. MHD-Valdis has previously been described in detail.[31] It dynamically couples the transient turbulent motion of each fluid layer and the interface shape to the transient magnetic field and electric currents in the cell.[31] The model includes essential commercial cell features, such as the electrolyte channels,[32] electric current distribution in the busbars, and the magnetic field generated by the ferromagnetic cell elements,[31] and has been validated against a benchmark model[33] and against measurements from the TRIMET 180 kA commercial potline[20] and other commercial cells[34,35]. A model of the same TRIMET cell is used in our stabilization study. MHD-Valdis uses the shallow-layer approximation in the Al and electrolyte layers, and utilizes a $k-\omega$ turbulence model. The electric boundary conditions used are zero normal current at the cell's side walls, a specified current density distribution at the anode and cathode blocks that change in time with the interface shape, continuity of electric potential across the Al–electrolyte interface, and continuity of the normal current component across the Al–electrolyte interface. Additionally, the hydrodynamic boundary conditions used are continuity of pressure across the Al–electrolyte interface, zero normal velocity at the side walls, and zero horizontal circulation velocity u_h at the side walls where u_h comes from decomposing the velocity field:

$$u(x,y,z,t) = u_h(x,y,t) + \epsilon u_w(x,y,z,t) + O(\epsilon^2) \quad (4)$$

where ϵ is a non-dimensional parameter that is the ratio of the wave amplitude to the depth of the fluid layers (assumed to be very small), and u_w is the wave-related velocity.

Simulation Protocol

The interface shape is initialized with the $G_{(1,0)}$ gravity mode as a perturbation with an amplitude of $\alpha_{(1,0)} = 5$ mm, similar to previous work,[20] and a steady and/or oscillating current with a specified frequency and amplitude. We use a 0.25-s time step and a numerical grid having $N_x \times N_y = 87 \times 31$ elements, so the grid size is 11.90×9.21 cm. Simulation is halted if the interface touches the anode, or after a set time has elapsed. A series of simulations were carried out with a purely steady current but at varying ACD to find its critical value for stability. At the critical ACD, the motion of a point on the interface has an amplitude that neither grows nor decays in time. We then ran a simulation at 5% below the critical ACD, and confirmed that the cell was unstable by observing the interface amplitude growing exponentially in time. When applying oscillating currents, we used a triangular shape (Fig. 6a) because it may be more economical to produce in real Al cells and because it eliminated the need for shorter time steps in simulations.

Projecting Onto Wave Modes

To express the interface displacement in terms of gravity wave modes, we used linear least-squares projection onto an orthonormal basis set formed from the $G_{(m,n)}$ modes defined in Eq. (1). In brief, linear least-squares projection is performed by determining the amplitudes $\alpha_{m,n}$ that minimize the squared error between the measured surface displacement and the surface displacement estimated using Eq. (1). We retained the 128 lowest-order modes $0 \le m \le 16$ and $0 \le n \le 8$. Spectral power in modes with $m > 6$ or $n > 6$ was always negligible. The $\alpha_{m,n}$ vary over time; one way to quantify their typical overall magnitude is with the RMS amplitude $\langle \alpha_{m,n} \rangle^{\frac{1}{2}}$, where brackets signify averaging over time.

Quantifying Surface Displacement

We calculated the RMS displacement of the surface from its mean as $\left(\frac{1}{N_x N_y}\sum_{i=1}^{N_x}\sum_{j=1}^{N_y}(z_{i,j} - \overline{z_{i,j}})^2\right)^{\frac{1}{2}}$, where the simulation grid has $N_x \times N_y$ elements, $z_{i,j}$ is the surface height of element (i,j), and $\overline{z_{i,j}}$ is its time-averaged height. When considering frequencies present in the surface displacement, we did not use the RMS, but rather used a single point in one corner of the cell, without squaring its displacement, since the square of a function generally contains different frequencies than the original function. We calculated power spectra using the fast Fourier transform.

ACKNOWLEDGEMENTS

The authors are grateful for fruitful discussions with Riccardo Betti, Curtis Broadbent, Gerrit M. Horstmann, and Jonathan S. Cheng.

CONFLICT OF INTEREST

The authors declare that they have no conflict of interest.

SUPPLEMENTARY INFORMATION

The online version contains supplementary material available at https://doi.org/10.1007/s11837-022-05254-8.

REFERENCES

1. I.A. Institute, *Aluminium sector greenhouse gas pathways to 2050* (IAI, 2021), https://international-aluminium.org/resource/aluminium-sector-greenhouse-gas-pathways-to-2050-2021/. Accessed from Jun 2021.
2. B. Gates, *How to Avoid a Climate Disaster: The Solutions We Have and the Breakthroughs We Need* (Alfred A Knopf, New york, 2021).
3. M. Gautam, B. Pandey, and M. Agrawal, *Environmental Carbon Footprints* (Elsevier, Amsterdam, 2018), p. 197.
4. P.A. Davidson, Mater. Sci. Technol. **16**, 475 (2000). https://doi.org/10.1179/026708300101508027.
5. T. Sele, Metall. Trans. B **8**, 613 (1977). https://doi.org/10.1007/BF02669338.
6. V. Bojarevics and M. Romerio, Eur. J. Mech. B **13**, 33 (1994).
7. P.A. Davidson, Eur. J. Mech. B **13**, 15 (1994).
8. P.A. Davidson and R.I. Lindsay, J. Fluid Mech. **362**, 273 (1998). https://doi.org/10.1017/S0022112098001025.
9. O. Zikanov, A. Thess, P.A. Davidson, and D.P. Ziegler, Metall. Trans. B **31B**, 1541 (2000). https://doi.org/10.1007/s11663-000-0039-6.
10. A. Lukyanov, G. El, and S. Molokov, Phys. Lett. A **290**, 165 (2001). https://doi.org/10.1016/S0375-9601(01)00653-3.
11. N. Urata, *Essential Readings in Light Metals* (Wiley, New Jersey, 2013), p. 373.
12. N. Urata, *Essential Readings in Light Metals* (Wiley, New Jersey, 2013), p. 330.
13. W. Herreman, C. Nore, J.-L. Guermond, L. Cappanera, N. Weber, and G.M. Horstmann, J. Fluid Mech. **878**, 598 (2019). https://doi.org/10.1017/jfm.2019.642.
14. G. Politis and J. Pried, J. Fluid Mech. **915**, A101 (2021). https://doi.org/10.1017/jfm.2021.100.
15. A. Pedcenko, S. Molokov, and B. Bardet, Metall. Trans. B **48**, 6 (2017). https://doi.org/10.1007/s11663-016-0840-5.
16. A.D. Sneyd and A. Wang, J. Fluid Mech. **263**, 343 (1994). https://doi.org/10.1017/S0022112094004143.
17. J. Gerbeau, C. Le Bris, and T. Lelièvre, *Mathematical Methods for the Magnetohydrodynamics of Liquid Metals* (Oxford University Press, Oxford, 2006), p. 251.
18. A. Lützerath, *Light Metals 2013* (TMS, Warrendale, 2013), p. 659.
19. M. Dupuis and V. Bojarevics, *Analyzing the impact on the cell stability power modulation on a scale of minutes* (Aluminium Smelting Industry, 2021), pp. 54–57. Accessed from Jun 2021.
20. V. Bojarevics and J.W. Evans, *Light Metals 2015* (TMS, Warrendale, 2015), p. 783.
21. D.H. Kelley and I. Mohammad, *Systems and methods for energy efficient electrolysis cells* (WIPO, 2021). https://patentscope.wipo.int/search/en/detail.jsf?docId=WO2021163142&_cid=P12-KTERWI-60301-1. Accessed from Jun 2021.
22. G.O. Linnerud and R. Huglen, *Method for electrical connection and magnetic compensation of aluminium reduction cells, and a system for same* (WIPO, 2006). https://patentscope.wipo.int/search/en/detail.jsf?docId=WO2006033578. Accessed from Jun 2021.
23. J. Chaffy, B. Langon, and M. Leroy, *Device for connection between very high intensity electrolysis cells for the production of aluminium comprising a supply circuit and an independent circuit for correcting the magnetic field*. https://patents.justia.com/inventor/joseph-chaffy. Accessed from Jun 2021.
24. M. Dupuis, A new aluminium electrolysis cell busbar network concept, ICSOBA (2015). http://www.genisim.com/download/A%20new%20aluminium%20electrolysis%20cell%20busbar%20network%20concept.pdf.
25. S. Akhmetov, J. Blasques, and M.I. Faraj, Potline retrofit to increase productivity under energy supply constraints. In: *12th Australasian Aluminium Smelting Technology Conference* (Queenstown, New Zealand, 2018).
26. N. Weber, P. Beckstein, W. Herreman, G.M. Horstmann, C. Nore, F. Stefani, and T. Weier, Phys. Fluids (2017). https://doi.org/10.1063/1.4982900.
27. G.M. Horstmann, N. Weber, and T. Weier, J. Fluid Mech. **845**, 1 (2018). https://doi.org/10.1017/jfm.2018.223.
28. O. Zikanov, Phys. Rev. E. **92**, 063021 (2015). https://doi.org/10.1103/PhysRevE.92.063021.
29. A. Allanore, L. Yin, and D.R. Sadoway, Nature **947**, 353 (2013). https://doi.org/10.1038/nature12134.
30. D. Sadoway, *Apparatus for electrolysis of molten oxides* (WIPO, 2008). https://patentscope.wipo.int/search/en/detail.jsf?docId=WO2008016526.
31. V. Bojarevics and K. Pericleous, Time dependent electric, magnetic and hydrodynamic interaction in aluminium electrolysis cells. In: *Fifth International Conference on CFD in the Process Industries* (Melbourne, 2006). https://www.cfd.com.au/cfd_conf06/PDFs/129Boj.pdf.
32. V. Bojarevicsa and K. Pericleous, *Jim Evans Honorary Symposium* (TMS, Warrendale, 2010), pp. 199–206.
33. V. Bojarevics and K. Pericleous, *Light Metals 2009* (TMS, Warrendale, 2009), pp. 569–574.
34. V. Bojarevics, E. Radionov, and Y. Tretiyakov, *Light Metals 2018* (TMS, Warrendale, 2018), pp. 551–556.
35. R. Shaoyong, Y. Feiya, M. Dupuis, V. Bojarevics, and Z. Jianfei, *Light Metals 2013* (TMS, Warrendale, 2013), pp. 603–607.